

## A SEARCH FOR $\text{Ly}\alpha$ EMISSION FROM THE ASTROSPHERE OF 40 ERIDANI A<sup>1</sup>

BRIAN E. WOOD,<sup>2</sup> JEFFREY L. LINSKY,<sup>2</sup> HANS-REINHARD MÜLLER,<sup>3,4</sup> AND GARY P. ZANK<sup>4</sup>

Received 2003 February 19; accepted 2003 March 21

### ABSTRACT

We report the results of *Hubble Space Telescope* (*HST*) observations of the nearby ( $d = 5.0$  pc) K1 V star 40 Eri A, which we use to search for scattered  $\text{Ly}\alpha$  emission surrounding the star indicative of the interaction between the stellar wind and the interstellar medium (ISM). Absorption from circumstellar hot H I has previously been detected around many solar-like stars in *HST* observations of their  $\text{Ly}\alpha$  lines, so there is potential for circumstellar  $\text{Ly}\alpha$  emission to be detectable as well. There was previously a tentative detection of absorption for 40 Eri A, but unfortunately, we do not detect any circumstellar emission around 40 Eri A in our new observations. We use hydrodynamic models of the stellar “astrosphere” (i.e., the ISM interaction region) and radiative transfer calculations to demonstrate that emission *should* have been detected for assumed mass-loss rates of  $\dot{M} \lesssim 2 \dot{M}_{\odot}$ , assuming that the star is surrounded by warm, partially neutral ISM material like that which surrounds the Sun. In contrast, when the models are compared with the absorption data, we find consistency with the data only for  $\dot{M} \gtrsim 2 \dot{M}_{\odot}$ . We believe that the most likely explanation for these apparently contradictory results is that the previous tentative detection of astrospheric absorption toward 40 Eri A is erroneous and that 40 Eri A probably lies within the hot ionized phase of the ISM. Thus, there is no interstellar H I within the astrosphere for us to detect in either absorption or emission, and no meaningful constraints on the mass-loss rate of 40 Eri A can be derived from the *HST* data.

*Subject headings:* hydrodynamics — radiative transfer — stars: individual (40 Eridani A) — stars: winds, outflows — ultraviolet: ISM — ultraviolet: stars

### 1. INTRODUCTION

Hydrodynamic models of our heliosphere predict that it should be filled with hot neutral hydrogen gas created by the collision between the solar wind and the surrounding interstellar medium (ISM) (Baranov & Malama 1993, 1995; Zank et al. 1996). Heliospheric  $\text{Ly}\alpha$  absorption from this hot H I has been detected in *Hubble Space Telescope* (*HST*) spectra (Linsky & Wood 1996; Izmodenov, Lallement, & Malama 1999). Absorption from analogous “astrospheric” H I surrounding many other solar-like stars has also been detected (Wood, Alexander, & Linsky 1996; Dring et al. 1997; Gayley et al. 1997; Wood & Linsky 1998; Wood, Linsky, & Zank 2000b). These astrospheric detections represent the first firm detections of solar-like winds around other dwarf stars. A wind detection for V471 Tau has also been claimed using a very different UV observational technique (Bond et al. 2001), although it is questionable whether the wind produced by this close, eclipsing K2 V+DA binary system is truly “solar-like” given the presence of the white dwarf companion. The astrospheric absorption has allowed the first mass-loss estimates to be made for solar-like stars, other than relatively loose upper limits (Wood et al. 2001; Müller, Zank, & Wood 2001a). These results have many important implications for our

understanding of stellar angular momentum evolution, the mass-loss history of the Sun, and the effects of the solar wind on the evolution of planetary atmospheres (Wood et al. 2002).

In principle, the astrospheric H I that is detected in absorption should also be observable in emission, since the H I will scatter stellar  $\text{Ly}\alpha$  photons, creating a nebula of  $\text{Ly}\alpha$  emission around the star. Observations of this emission would provide valuable new information on the stellar wind and its interaction with the ISM. The absorption data only indicate the astrospheric properties along our line of sight to the star, but astrospheric emission would supply information about the spatial structure and full extent of the astrosphere, thereby providing new constraints for the models that are used to extract mass-loss measurements from the *HST* data. An emission detection, for example, would allow a direct measurement of the distance to the stellar bow shock, which is something that is not known observationally even for our own heliosphere. For these reasons, we proposed an observing program to detect astrospheric  $\text{Ly}\alpha$  emission around a nearby star.

A prerequisite for astrospheric  $\text{Ly}\alpha$  emission or absorption to be detectable around a star is that the star must be surrounded by interstellar material that is at least partially neutral. If there is no neutral hydrogen in the surrounding ISM, there is no  $\text{Ly}\alpha$  emission or absorption to be detected. However, the Sun lies inside a region of space called the “Local Bubble,” in which most of the volume consists of hot ( $T \sim 10^6$  K), ionized gas (e.g., Sfeir et al. 1999). There are small, partially neutral clouds embedded within the Local Bubble, and the Sun lies within one of these. However, many nearby stars will reside within the hot ISM rather than the warm, partially neutral ISM. For this reason, when looking for potential targets to detect astrospheric emission we focused on stars that have had at least tentative detections of astrospheric absorption (see Wood et

<sup>1</sup> Based on observations with the NASA/ESA *Hubble Space Telescope*, obtained at the Space Telescope Science Institute, which is operated by the Association of Universities for Research in Astronomy, Inc., under NASA contract NAS5-26555.

<sup>2</sup> Joint Institute for Laboratory Astrophysics, University of Colorado and National Institute for Standards and Technology, Boulder, CO 80309-0440; woodb@origins.colorado.edu, jlinsky@jila.colorado.edu.

<sup>3</sup> Department of Physics and Astronomy, Dartmouth College, 6127 Wilder Lab, Hanover, NH 03755-3528; hans.mueller@dartmouth.edu.

<sup>4</sup> Institute of Geophysics and Planetary Physics, University of California, 1432 Geology, Riverside, CA 92521; zank@ucr1.ucr.edu.

al. 2002), since such detections presumably remove this ISM ionization state concern.

Unfortunately, crude surface brightness estimates suggest that the astrospheric Ly $\alpha$  emission should generally be quite faint, because astrospheres are rather large structures and the stellar Ly $\alpha$  light is therefore scattered over a wide area. Of the stars with detected astrospheric absorption, the only potential targets are the two stars expected to have the most compact astrospheres: 61 Cyg A and 40 Eri A. The primary reason the astrospheres of these stars are expected to be compact is because of the high interstellar wind velocities seen by these stars: 86 and 127 km s $^{-1}$  for 61 Cyg A and 40 Eri A, respectively, compared with the 26 km s $^{-1}$  ISM flow velocity seen by the Sun. We chose the K1 V star 40 Eri A as our target star to search for astrospheric emission since it sees the highest ISM velocity (127 km s $^{-1}$ ), but this choice does have one significant downside, and that is that the astrospheric absorption detection for 40 Eri A from Wood & Linsky (1998) is questionable (Wood et al. 2002). Nevertheless, 40 Eri A was our choice, and in this paper we report on the results of our attempt to detect astrospheric emission surrounding this star.

In § 2, we briefly review the analysis of the old Ly $\alpha$  absorption data for 40 Eri A. In § 3, we present the new *HST* observations of 40 Eri A, in which we attempt to detect astrospheric emission around the star. In § 4, we present hydrodynamic models of the 40 Eri A astrosphere, which are used to predict how much astrospheric Ly $\alpha$  emission and absorption we should see as a function of mass-loss rate. In § 5, we compare the absorption predictions with the absorption data, and then based on radiative transfer calculations presented in § 6, we compare emission predictions with the new *HST* data in § 7. Finally, in § 8 we discuss and summarize our findings.

## 2. OLD *HST*/GODDARD HIGH RESOLUTION SPECTROGRAPH OBSERVATIONS OF 40 ERI A

On 1997 January 28, the Goddard High Resolution Spectrograph (GHRS) instrument on *HST* was used to observe the H I Ly $\alpha$  emission line of 40 Eri A. Wood & Linsky (1998) showed that the absorption seen in the observed Ly $\alpha$  profile can be fitted with interstellar absorption alone, but when the wings of the emission line are forced to be centered on the stellar rest frame, the resulting fit suggests a suspiciously low deuterium-to-hydrogen ratio (D/H) of  $(1.11 \pm 0.09) \times 10^{-5}$ . This is significantly lower than the canonical local ISM value of D/H =  $1.5 \times 10^{-5}$  (Linsky 1998; Moos et al. 2002).

An alternative way of fitting the data assuming D/H =  $1.5 \times 10^{-5}$  is to add a very broad, unsaturated astrospheric absorption component to the fit. Since one might expect 40 Eri A to have an astrospheric absorption component similar to this, Wood & Linsky (1998) presented that as their best fit to the data. However, the evidence for this astrospheric absorption is much weaker than is the case for the other astrospheric detections, because it relies on the D/H =  $1.5 \times 10^{-5}$  assumption and the ability to accurately establish the centroid of the Ly $\alpha$  line wings, despite the low signal-to-noise ratio in the far wings of the line. Furthermore, the extremely broad, unsaturated nature of the astrospheric absorption component tentatively identified for 40 Eri A is very different from the narrower and very saturated

astrospheric absorption components detected for other stars, and such an absorption component will be intrinsically harder to detect. Thus, in their compilation of astrospheric detections, Wood et al. (2002) flagged the 40 Eri A detection as uncertain.

Mass-loss rates have been estimated for all stars with detected astrospheric absorption, based on comparing the observed Ly $\alpha$  absorption with that predicted by astrospheric models assuming various mass-loss rates, but Wood et al. (2002) had difficulty making such an estimate for 40 Eri A. In addition to being an uncertain detection, the unsaturated nature of the astrospheric absorption toward 40 Eri A makes it possible for almost any model to fit the data if suitable alterations are made to the intrinsic stellar Ly $\alpha$  line profile assumed for 40 Eri A. Nevertheless, for sufficiently high mass-loss rates, the amount of astrospheric absorption predicted by the models becomes too high for this to work, so Wood et al. (2002) quote an upper limit for 40 Eri A's mass-loss rate of 5 times the solar mass-loss rate (i.e.,  $\dot{M} < 5 \dot{M}_{\odot}$ , where  $\dot{M}_{\odot} \approx 2 \times 10^{-14} M_{\odot} \text{ yr}^{-1}$ ). Using additional models we will refine this analysis in § 5.

## 3. NEW *HST*/SPACE TELESCOPE IMAGING SPECTROMETER OBSERVATIONS OF 40 ERI A

The Space Telescope Imaging Spectrometer (STIS) on board *HST*, which replaced the GHRS in 1997, is the instrument we use to search for H I Ly $\alpha$  emission surrounding 40 Eri A. Unfortunately, we cannot simply take a UV image of 40 Eri A and detect the astrospheric emission in that way, because the faint circumstellar emission will be overwhelmed by the bright geocoronal Ly $\alpha$  background. To minimize this problem, we observed 40 Eri A using long-slit spectroscopy, with the expectation that the astrospheric emission will be broad enough to extend at least partly beyond the narrow geocoronal Ly $\alpha$  emission profile. This hopefully allows a detection of the astrospheric emission while still providing information about the spatial distribution of the astrospheric H I along the slit axis. In order to minimize the geocoronal emission, our observations on 2001 January 26 were performed during “shadow time,” with the *HST* within the Earth's shadow and with the telescope pointed away from the Earth to the greatest extent possible. We used the 52"  $\times$  0.2 F1 long slit, which has an occulting bar that we placed over the star to minimize scattered starlight. The G140M grating was used to observe the Ly $\alpha$  spectral region. The total exposure time of our observation was 7814 s, and the data were processed using the IDL-based CALSTIS software package (Lindler 1999).

Figure 1a shows the long-slit *HST*/STIS image, rebinned by a factor of 10 in the spatial direction. The spatial axis is in units of AU from the star, where positive distances correspond to the upwind ISM direction from the star. It is in the upwind direction where we expect the astrospheric emission to be brightest. The bright vertical emission stripe is geocoronal emission, which fills the long slit. There is no obvious excess in the upwind direction that would indicate the presence of astrospheric emission. We estimate the average shape of the geocoronal profile far from the star in the downwind direction, where little astrospheric emission is expected, and then subtract this profile at all spatial locations to try to remove the geocoronal emission. The resulting image in Figure 1b after this subtraction shows

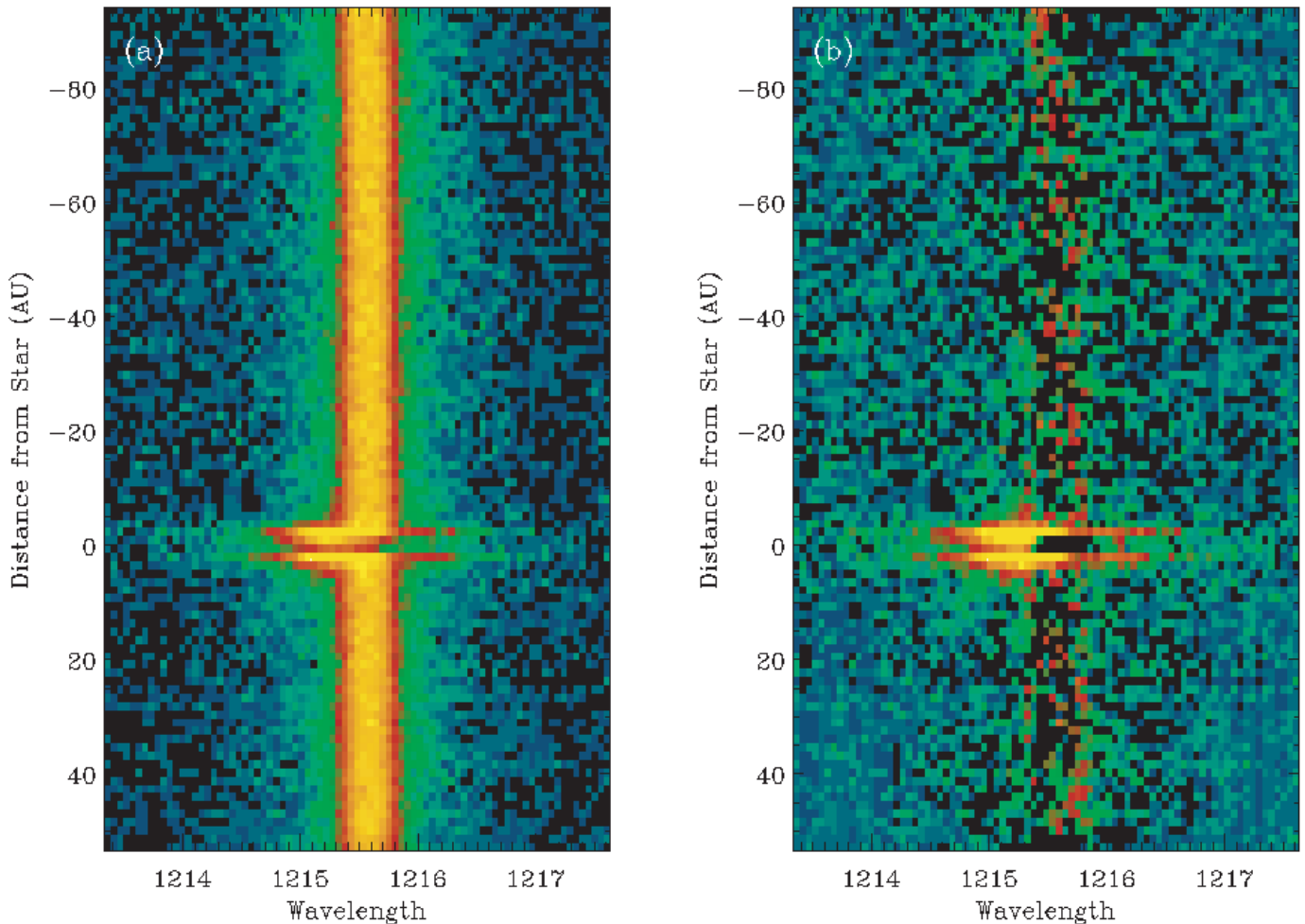


FIG. 1.—(a) *HST/STIS* long-slit Ly $\alpha$  spectrum of 40 Eri A. The bright vertical stripe is geocoronal emission. An occulting bar overlies the star at 0 AU. The y-axis gives the distance from the star, where positive numbers are for the upwind direction of the ISM flow seen by the star and the x-axis is the wavelength in Å. (b) *HST/STIS* data after subtraction of the geocoronal emission. There is no remaining emission that would represent a detection of circumstellar, astrospheric H I. The emission near 0 AU is just the stellar emission extending beyond the occulting bar.

that no obvious emission remains. The apparent excess near 0 AU is just the stellar Ly $\alpha$  profile extending beyond the occulting bar, indicative of the point-spread function of the telescope and STIS. *Our conclusion is that there is no astrospheric emission detected in our HST/STIS observations.*

#### 4. HYDRODYNAMIC MODELS OF THE 40 ERI A ASTROSPHERE

Modeling is required to determine what the nondetection of astrospheric emission implies for the mass-loss rate of 40 Eri A and to see whether the nondetection is inconsistent with the tentative detection of astrospheric absorption by Wood & Linsky (1998). The first step is to create hydrodynamic models of the 40 Eri A astrosphere assuming different stellar mass-loss rates, as was previously done for all stars with detected astrospheric absorption (Wood et al. 2002). We use the two-dimensional axisymmetric four-fluid code of Zank et al. (1996) for this purpose. In this code, the wind-ISM interaction is approximated as the interaction between four separate fluid components: one plasma component and three neutral components. The three neutral components correspond to three distinct regions in which

neutrals are created by charge exchange processes. Component 1 represents undisturbed interstellar neutrals and neutrals created by charge exchange between the stellar bow shock and “astropause” (analogous to the Sun’s “heliopause”). Components 2 and 3 consist of H I created by a charge exchange between the termination shock and astropause and H I created inside the termination shock, respectively. Component 1 is by far the dominant component, although the presence of the other two components can have noticeable effects on the heliospheric/astrospheric structures (Zank et al. 1996; Müller et al. 2001).

The 40 Eri A astrospheric models are extrapolated from a heliospheric model that successfully reproduces heliospheric Ly $\alpha$  absorption for several lines of sight (model 10 from Wood, Müller, & Zank 2000c). All parameters in the astrospheric models are the same as in this heliospheric model except for the ISM wind speed, which is  $V_{\text{ISM}} = 127 \text{ km s}^{-1}$  rather than the solar  $V_{\text{ISM}} = 26 \text{ km s}^{-1}$  value (see Wood et al. 2002), and the stellar wind density, which is varied to assume different mass-loss rates. Four-fluid models created in this manner have been used to successfully reproduce astrospheric Ly $\alpha$  absorption observed for many stars, yielding estimates of stellar mass-loss rates (Müller et al. 2001;

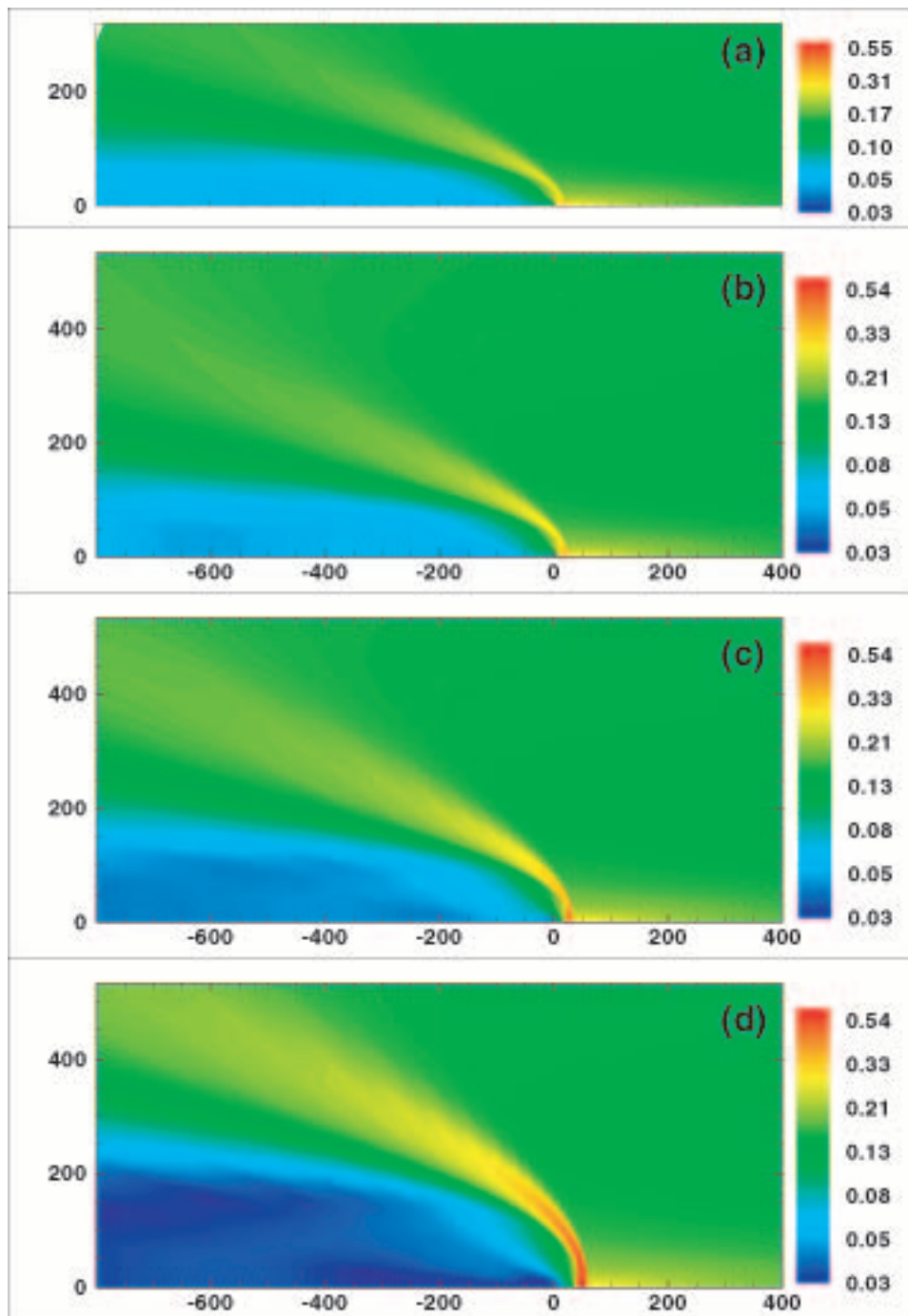


FIG. 2.—Distribution of H I density (in  $\text{cm}^{-3}$ ) predicted by four hydrodynamic models of the 40 Eri A astrosphere. The distance scale is in units of AU. The stellar mass-loss rates assumed for the four models are (a) 0.5, (b) 1, (c) 2, and (d)  $5 \dot{M}_{\odot}$ , where  $1 \dot{M}_{\odot} \approx 2 \times 10^{-14} M_{\odot} \text{ yr}^{-1}$ .

Wood et al. 2001, 2002). Figure 2 shows H I density maps for four 40 Eri A models computed assuming mass-loss rates of 0.5, 1, 2, and  $5 \dot{M}_{\odot}$ . The models also provide distributions of temperature and flow velocity. All the models show a density enhancement between the astropause and bow shock, which has been called the “hydrogen wall.” The size of the astrosphere and thickness of the hydrogen wall naturally increase with increasing mass-loss rates. The models show a high-density projection in front of the bow shock. This is due to neutral H particles created by charge exchange

very near the stagnation point where flow velocities fall to zero. The thermal velocities of new neutrals created there dominate their flow velocities, which allow them to travel back upwind.

#### 5. COMPARISON OF MODEL PREDICTIONS WITH THE ABSORPTION DATA

Before determining what the models presented in § 4 predict for the astrospheric Ly $\alpha$  emission around 40 Eri

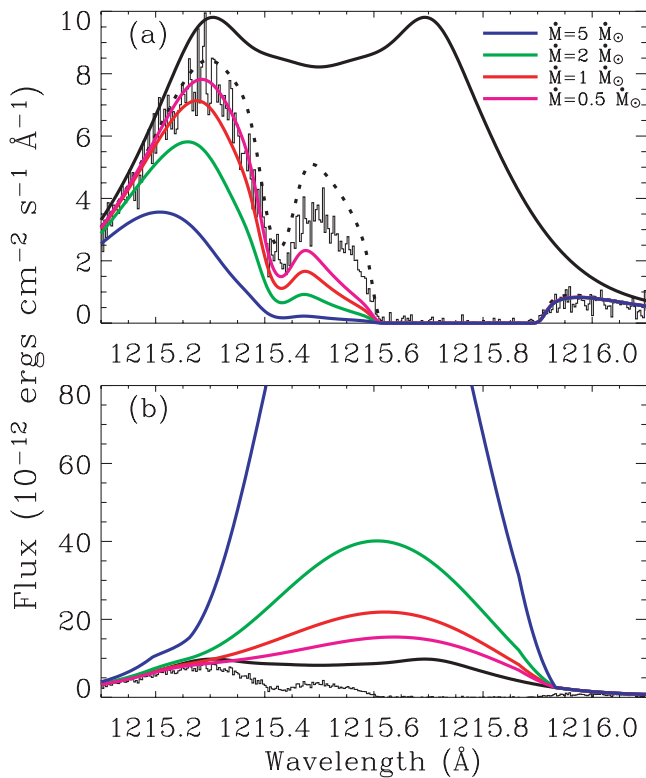


Fig. 3.—(a) *HST* Ly $\alpha$  spectrum of 40 Eri A (histogram), showing broad H I absorption at 1215.8 Å and narrow D I absorption at 1215.4 Å. The top solid line is the assumed intrinsic stellar emission line, and the dotted line shows the Ly $\alpha$  profile after only ISM absorption. The excess H I absorption on the blue side of the line is astrospheric absorption. Colored lines show the predicted astrospheric absorption from four astrospheric models with mass-loss rates in the range  $\dot{M} = 0.5\text{--}5 M_{\odot}$ . The models all predict too much absorption when compared with the data, which can be remedied by increasing the flux of the assumed stellar Ly $\alpha$  emission profile, and panel (b) shows the four profiles that must be assumed to make the four models fit the data. The smooth black line is the original assumed stellar profile from (a).

A, we first see what they predict for Ly $\alpha$  absorption toward 40 Eri A. Wood et al. (2002) have already done this for the 1 and 5  $M_{\odot}$  models. We refine their results here using the two additional models and a more extensive analysis, although we refer the reader to the previous paper for a more detailed discussion of this technique for mass-loss estimation and the systematic errors involved.

The Ly $\alpha$  spectrum observed toward 40 Eri A is shown in Figure 3a along with Wood & Linsky's (1998) best estimate of the intrinsic stellar Ly $\alpha$  emission profile, and their best estimate of the profile after interstellar absorption alone is considered (dotted line). (Note that we have removed the geocoronal absorption from the data based on their analysis.) Wood et al. (2002) estimate the line of sight from the star toward the Sun to be 59° from the upwind direction of the stellar astrosphere. The Ly $\alpha$  absorption predicted for this line of sight by the four models in Figure 2 is shown as colored lines in Figure 3a, after being added to the ISM absorption. All four models appear to predict too much absorption. However, thanks to the very broad, unsaturated nature of the astrospheric absorption it is possible to change the assumed stellar profile to improve the fit to the data (see § 2 and Wood et al. 2002), and Figure 3b shows the four

revised stellar Ly $\alpha$  emission profiles that must be assumed for the four models to fit. The more a model overpredicts the absorption in Figure 3a, the more the assumed stellar profile must be revised upward to make the model fit the data. However, it is highly questionable whether some of the profiles in Figure 3b are truly reasonable representations of the real stellar Ly $\alpha$  emission profile. The very steep, narrow, and tall profile required to make the 5  $M_{\odot}$  model work is particularly unlikely based on comparisons with other stellar (and solar) Ly $\alpha$  profiles (e.g., Linsky & Wood 1996; Piskunov et al. 1997; Wood et al. 2000a).

In order to make a more objective determination of how reasonable the stellar Ly $\alpha$  profiles in Figure 3b are, in Figure 4 we divide the integrated fluxes of these profiles by the Mg II *h* and *k* line-emission fluxes and compare these Ly $\alpha$ /Mg II ratios with those of other K dwarf stars. We use data from Wood et al. (2000a), who list Ly $\alpha$  and Mg II fluxes for many early K dwarfs, including 40 Eri A (see their Table 5). The stellar Mg II *h* and *k* lines at 2803 and 2796 Å, respectively, are formed at similar chromospheric temperatures as Ly $\alpha$ . One would therefore expect the Ly $\alpha$ /Mg II ratios to be similar for all K dwarfs, although some variations are to be expected from Mg abundance differences.

In Figure 4, we plot the ratios as a function of rotation period to see whether there is a dependence on rotation that needs to be accounted for. There is no clear dependence on rotation for the full sample of stars from Wood et al. (2000a). However, the observed Ly $\alpha$ /Mg II ratios all fall in the range 0.39–1.29. For comparison, the value for 40 Eri A, assuming the best initial estimate of the 40 Eri A stellar Ly $\alpha$  profile, is 0.60, but this value rises when the profile is altered to correct for the astrospheric absorption predicted by the models. The 0.5 and 1  $M_{\odot}$  models yield Ly $\alpha$ /Mg II ratios that are within the range of observed values, but the ratios

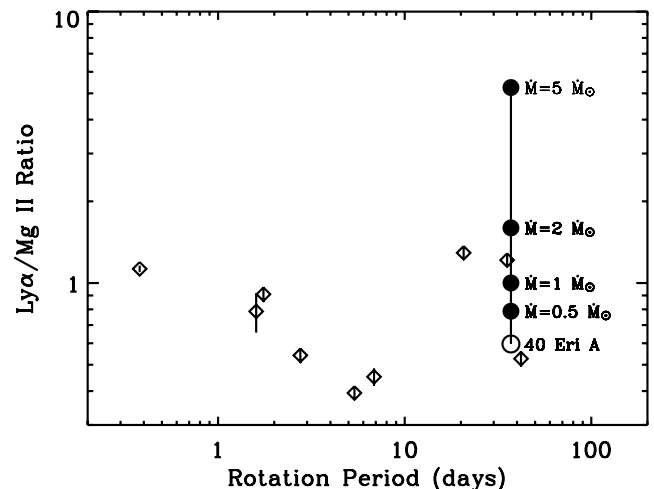


Fig. 4.—Ratio of H I Ly $\alpha$  fluxes to Mg II *h* and *k* fluxes for early K dwarfs (diamonds) plotted vs. stellar rotation period, using data from Wood et al. (2000a). The open circle shows the Ly $\alpha$ /Mg II ratio for 40 Eri A using the original, best-estimate Ly $\alpha$  profile from Wood & Linsky (1998), while the filled circles show ratios computed for 40 Eri A using the revised 40 Eri A Ly $\alpha$  profiles from Fig. 3b based on corrections for astrospheric absorption assuming different mass-loss rates. The 0.5 and 1  $M_{\odot}$  models yield Ly $\alpha$ /Mg II ratios consistent with those seen for the other stars, while the 2 and 5  $M_{\odot}$  models yield ratios that are too high.

suggested by the 2 and 5  $\dot{M}_\odot$  models are noticeably higher (see Fig. 4). Thus, we quote an upper limit of  $\dot{M} \lesssim 2 \dot{M}_\odot$  based on these results. This is a revision of the  $\dot{M} < 5 \dot{M}_\odot$  result from Wood et al. (2002).

## 6. RADIATIVE TRANSFER MODELING OF THE 40 ERI A ASTROSPHERE

We use the 40 Eri A models shown in Figure 2 as the basis for generating simulated images of the astrosphere in scattered stellar Ly $\alpha$  light. Because the astrospheric structure exhibits neither planar nor spherical symmetry, the radiative transfer (RT) must essentially be done in three dimensions, making it a complicated problem. However, there *is* cylindrical symmetry. Figure 5 shows the radial grid of points we use in the RT modeling of the 1  $\dot{M}_\odot$  astrosphere. This grid is rotated about the  $x$ -axis, so each bin in Figure 5 is actually an annulus centered on the  $x$ -axis. The red lines in Figure 5 show examples of photon tracks through the grid for 20 different  $\phi$  angles and 5 different  $\theta$  angles, where  $\phi$  is the orientation angle in the plane of the figure and  $\theta$  is the angle out of the plane. The five  $\theta$  angles are chosen so that the angle bins represent equal solid angles into which a photon might scatter.

To make the RT problem tractable, we limit the photon scattering to the 20  $\phi$  and 5  $\theta$  angles shown in Figure 5, which we compute for each bin, allowing us to determine the trace of density, temperature, velocity, and finally wavelength-dependent opacity along all possible photon tracks before using a Monte Carlo routine to actually follow Ly $\alpha$  photons through the grid. The advantage of this approach is that one does not have to recompute the opac-

ities a photon sees after each scattering event sends it in a different direction. This greatly lowers the computing time. The disadvantage of predefined photon tracks is that the opacity array that must be stored before starting the Monte Carlo part of the computation is huge. Memory constraints therefore limit us to fairly coarse grids, as in Figure 5. Nor are we able to greatly increase the number of  $\phi$  and  $\theta$  angles without violating memory constraints.

The Monte Carlo part of the radiative transfer calculation is based on a plane-parallel code from Wood & Karovska (2000) that was previously used for other purposes. In the Monte Carlo routine, we inject stellar Ly $\alpha$  photons at the star's location at the center of the grid in Figure 5 assuming the stellar Ly $\alpha$  profile from Wood & Linsky (1998) to establish the initial wavelength distribution of the injected photons. We then follow the photons one by one to see where they scatter, allowing us to build up a source function,  $S_\lambda$ , at each location in the grid.

For each scattering event, we assume partial frequency redistribution (PRD), but we assume complete angular redistribution into the  $\phi$  and  $\theta$  angles mentioned above. The PRD treatment is described in detail by Wood & Karovska (2000). The very low densities that are present in the astrosphere mean that the redistribution function can be assumed to be  $R_{II}$ , an integral function first defined by Hummer (1962). Rather than use one of many approximations that have been developed for computing  $R_{II}$  (e.g., Adams, Hummer, & Rybicki 1971; Kneer 1975), we evaluate  $R_{II}$  by direct numerical integration.

Once the Monte Carlo part of the computation is complete and we have a grid of source functions, we can compute the intensity that an observer would see from all

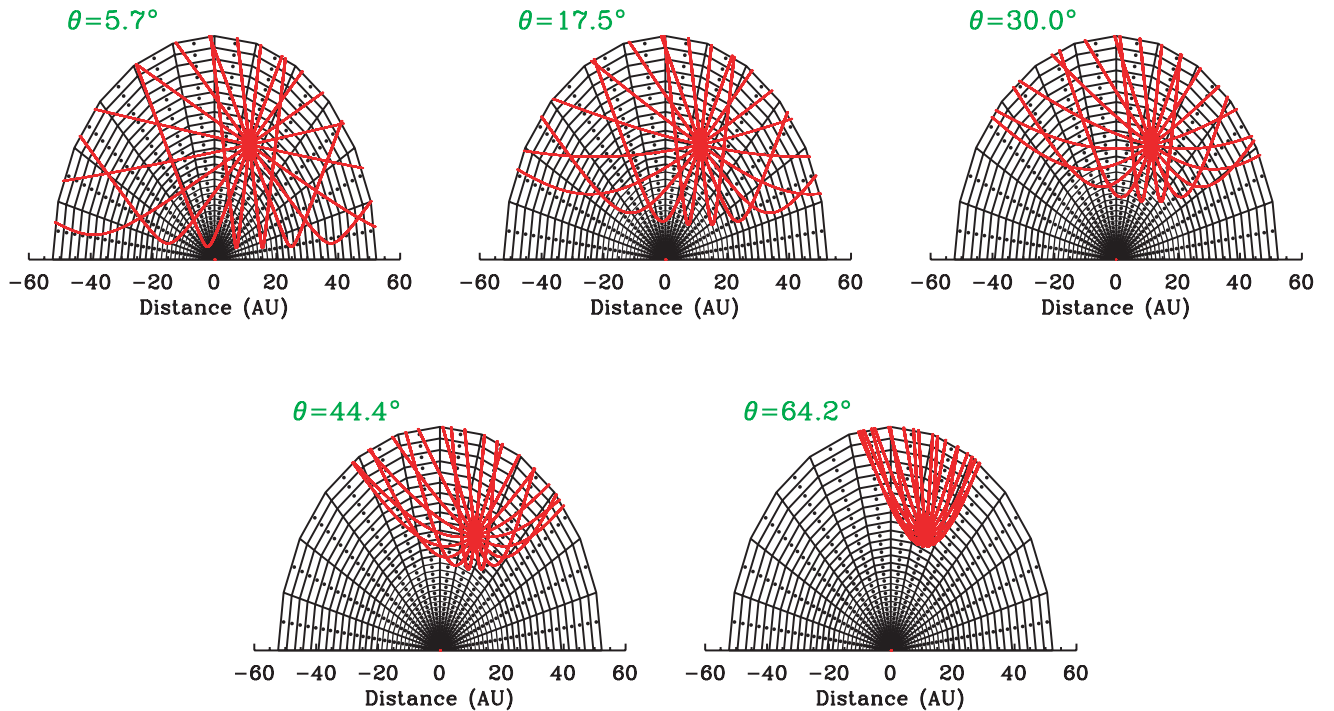


FIG. 5.—Illustration of the grid used in the Monte Carlo radiative transfer calculations for the 1  $\dot{M}_\odot$  40 Eri A model in Fig. 2. The actual three-dimensional grid is the illustrated two-dimensional grid rotated about the  $x$ -axis, meaning that each bin is an annulus centered on the  $x$ -axis. Red lines show examples of three-dimensional photon trajectories projected into the two-dimensional representation of the grid for 20  $\phi$  angles within the plane of the figure and for 5  $\theta$  angles for the angle out of the plane of the figure.

parts of the astrosphere, from any perspective. The intensity seen from a direction with an opacity vector through the astrosphere of  $\tau_\lambda$  is simply

$$I_\lambda = \int_0^{\tau_\lambda} S_\lambda(t) e^{-t} dt. \quad (1)$$

By creating a square grid of these intensities, we can generate simulated images of the astrosphere, viewed from any orientation angle. Simulated Ly $\alpha$  spectra can also be computed for each location in the image. We include corrections for ISM absorption using the best-fit ISM parameters for the 40 Eri A line of sight measured by Wood & Linsky (1998):  $\log N_{\text{H I}} = 17.85$ ,  $b_{\text{H I}} = 11.6 \text{ km s}^{-1}$ ,  $V_{\text{H I}} = 21.4 \text{ km s}^{-1}$ , and  $D/H = 1.5 \times 10^{-5}$ .

One complication that has not been addressed is that the hydrodynamic models actually consist of three distinct H I components that all permeate the entire astrosphere, each with its own temperature, density, and flow velocity distribution. As mentioned in § 4, the component 1 neutrals dominate. In our RT calculations we completely ignore the very low density component 3 neutrals, which are created by charge exchange within the termination shock, but we do include the component 2 neutrals, which are created by charge exchange processes between the termination shock and astropause.

Every time a photon scatters in our Monte Carlo RT code, it is first determined which of the two components (component 1 or 2) does the scattering, with the odds computed based on comparing the relative opacity of the two components at the location of the scattering. The new frequency of the scattered photon is then computed based on the redistribution function appropriate for the component responsible for the scattering. Separate source functions are accumulated for the two components, and in generating simulated images and spectra we sum up the intensities computed using equation (1) for both components. We find, however, that the Ly $\alpha$  intensities generated by the component 2 neutrals are low enough that they could have been ignored along with those of component 3. Thus, the scattered Ly $\alpha$  light in the simulated images and spectra presented in § 7 is almost entirely from the component 1 neutrals.

## 7. SIMULATED IMAGES AND SPECTRA OF THE 40 ERI A ASTROSPHERE

If the 40 Eri A astrosphere is observed from a sidewind direction, as portrayed in Figure 2, then Figure 6 shows the surface brightnesses that we predict should be observed directly upwind and downwind of the star (relative to the ISM flow) based on our four models. The intensities naturally tend to be peaked at the star's location, since that is where the Ly $\alpha$  photons originate, and at the location of the hydrogen wall, as that is where H I densities are highest and the Ly $\alpha$  scattering is greatest. The stellar peak dominates for the low mass-loss rate models, but the hydrogen wall peak becomes dominant for the more opaque, higher mass-loss rate models. The most important thing to note about Figure 6 is that the average surface brightness decreases with increasing mass-loss rates. This somewhat counter-intuitive result is simply due to the Ly $\alpha$  emission being scattered over a much larger astrosphere for the higher mass-loss rate models. Since all of the model astrospheres

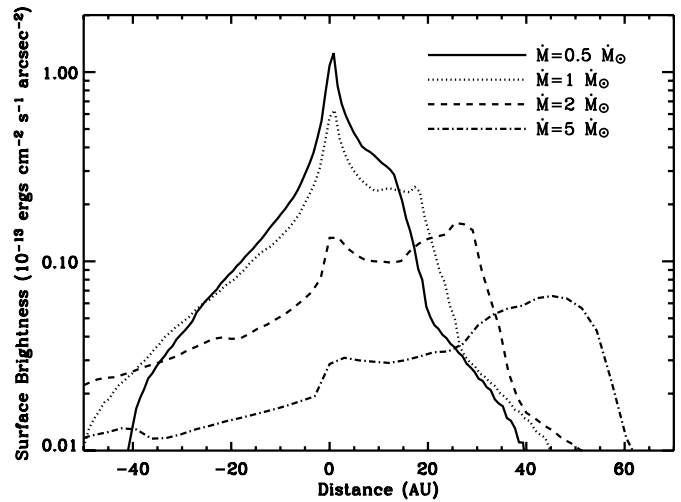


FIG. 6.—Predicted surface brightness tracings of Ly $\alpha$  emission directly upwind (*positive distances*) and downwind (*negative distances*) from 40 Eri A, based on the models of the 40 Eri A astrosphere shown in Fig. 2 assuming four different mass-loss rates. The surface brightnesses are computed assuming that the astrosphere is observed from a sidewind orientation, as portrayed in Fig. 2.

are fairly optically thick to Ly $\alpha$  emission, they all scatter roughly the same amount of Ly $\alpha$  photons, but this scattered light is spread over a larger surface area for the larger astrospheres. (The 1, 2, and 5  $M_\odot$  models actually scatter 13%, 33%, and 52% more photons, respectively, than the 0.5  $M_\odot$  model.) In contrast, astrospheric absorption will always *increase* with increasing mass-loss rates, since the astrospheric H I column density will increase.

Based on our knowledge of the stellar motion vector and the local ISM flow vector, our actual viewing angle of the 40 Eri A astrosphere is 59° from the upwind direction seen by the star (Wood et al. 2002). Figure 7 shows simulated images of the astrosphere for our four models as viewed from that angle. Superposed on the images is the 52"  $\times$  0".2 slit used in our *HST*/STIS observations of the astrosphere. As shown in the figure, the slit is oriented 14:1 from the direction of the ISM flow seen by the star. For the 5  $M_\odot$  model, the slit barely reaches the brightest part of the hydrogen wall. Because each of the images is on its own independent color scale, the decrease in intensity with increasing mass loss discussed above (as shown in Fig. 6) is not apparent, although one *can* see the increasing prominence of emission from the hydrogen wall as the mass-loss rate is increased.

From the simulated images shown in Figure 7, we can compute a Ly $\alpha$  spectrum for each point along the STIS slit, for comparison with the STIS data. In Figure 8, we add the model Ly $\alpha$  spectra to our best estimate of the geocoronal profile (*solid line*) and compare with the data for eight points along the slit. The data show no excess emission above the geocoronal profile that would suggest detected astrospheric emission. The excess near the star (at  $\pm 5$  AU) is just from the wings of the unscattered stellar profile (see § 3).

With Figure 8 we can finally address the fundamental question that motivates our modeling efforts: Should our *HST* observations have been able to detect astrospheric emission from 40 Eri A? For the 0.5 and 1  $M_\odot$  models we believe the answer is clearly “yes,” as these models appear

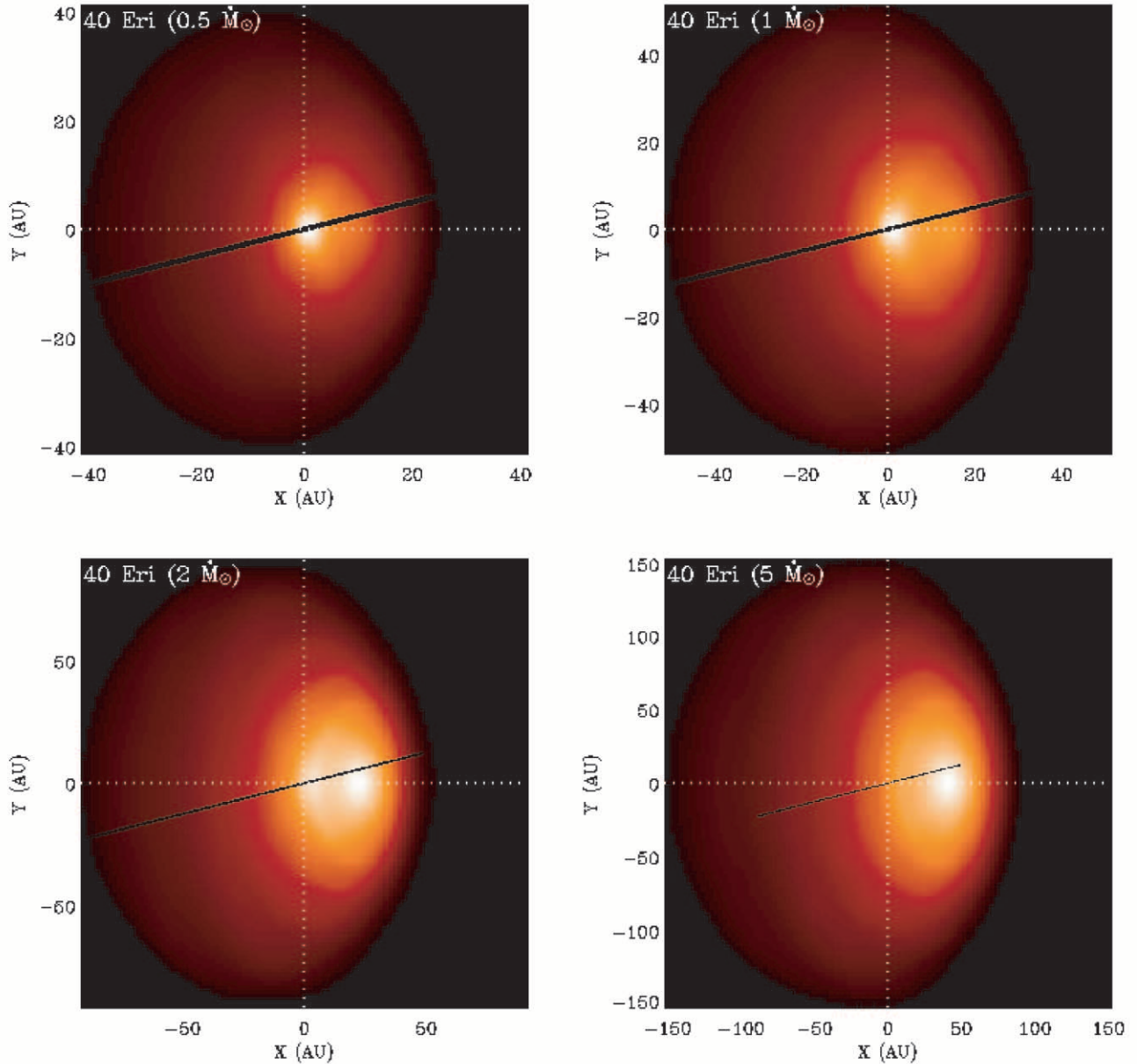


FIG. 7.—Simulated Ly $\alpha$  images of the 40 Eri A astrosphere as seen from our viewing angle  $59^\circ$  from the upwind direction of the ISM flow, for the four models shown in Fig. 2. Superposed on the images is the *HST*/STIS long slit used to try to detect this astrospheric emission, which is oriented  $14.1^\circ$  from the upwind direction. Note that the slit does not extend all the way through the emission for the  $5 \dot{M}_\odot$  model.

to predict a significant amount of excess emission on the red side of the geocoronal emission line at the 5–15 AU location. The case for the  $2 \dot{M}_\odot$  model is more marginal, but we believe this model also predicts a detectable amount of excess emission at 15–25 AU.

In order to better quantify this, one can compare the excess flux above the geocoronal profile that is observed with that predicted by the models between 1215.9 and 1216.15 Å, where the models suggest the greatest excess. At the 15 AU location, for example, the excess fluxes predicted by the  $0.5$ ,  $1$ ,  $2$ , and  $5 \dot{M}_\odot$  models are  $5.2 \times 10^{-15}$ ,  $5.3 \times 10^{-15}$ ,  $3.0 \times 10^{-15}$ , and  $1.7 \times 10^{-15}$  ergs cm $^{-2}$  s $^{-1}$  arcsec $^{-2}$ , respectively, while the observed excess is  $(-1.1 \pm 1.2) \times 10^{-15}$  ergs cm $^{-2}$  s $^{-1}$  arcsec $^{-2}$ . The uncertainty in the observed flux indicates that the excesses predicted by the  $0.5$ ,  $1$ ,  $2$ , and  $5 \dot{M}_\odot$  models should have been

detected at confidence levels of 4.3, 4.4, 2.5, and 1.4  $\sigma$ , respectively. These calculations support our visual conclusions from Figure 8 that the  $0.5$ – $2 \dot{M}_\odot$  models predict that we should have detected emission, although the case for the  $2 \dot{M}_\odot$  model is somewhat marginal. Thus, the data-model comparison with the emission data lead us to limit allowable mass-loss rates to  $\dot{M} \gtrsim 2 \dot{M}_\odot$ , which contradicts the earlier result from the data-model comparison with the absorption data,  $\dot{M} \lesssim 2 \dot{M}_\odot$  (see § 5).

## 8. DISCUSSION AND CONCLUSIONS

We have presented in this paper new *HST*/STIS observations of 40 Eri A obtained to search for circumstellar Ly $\alpha$  emission associated with the star’s wind-ISM interaction region, i.e., its astrosphere. These observations complement

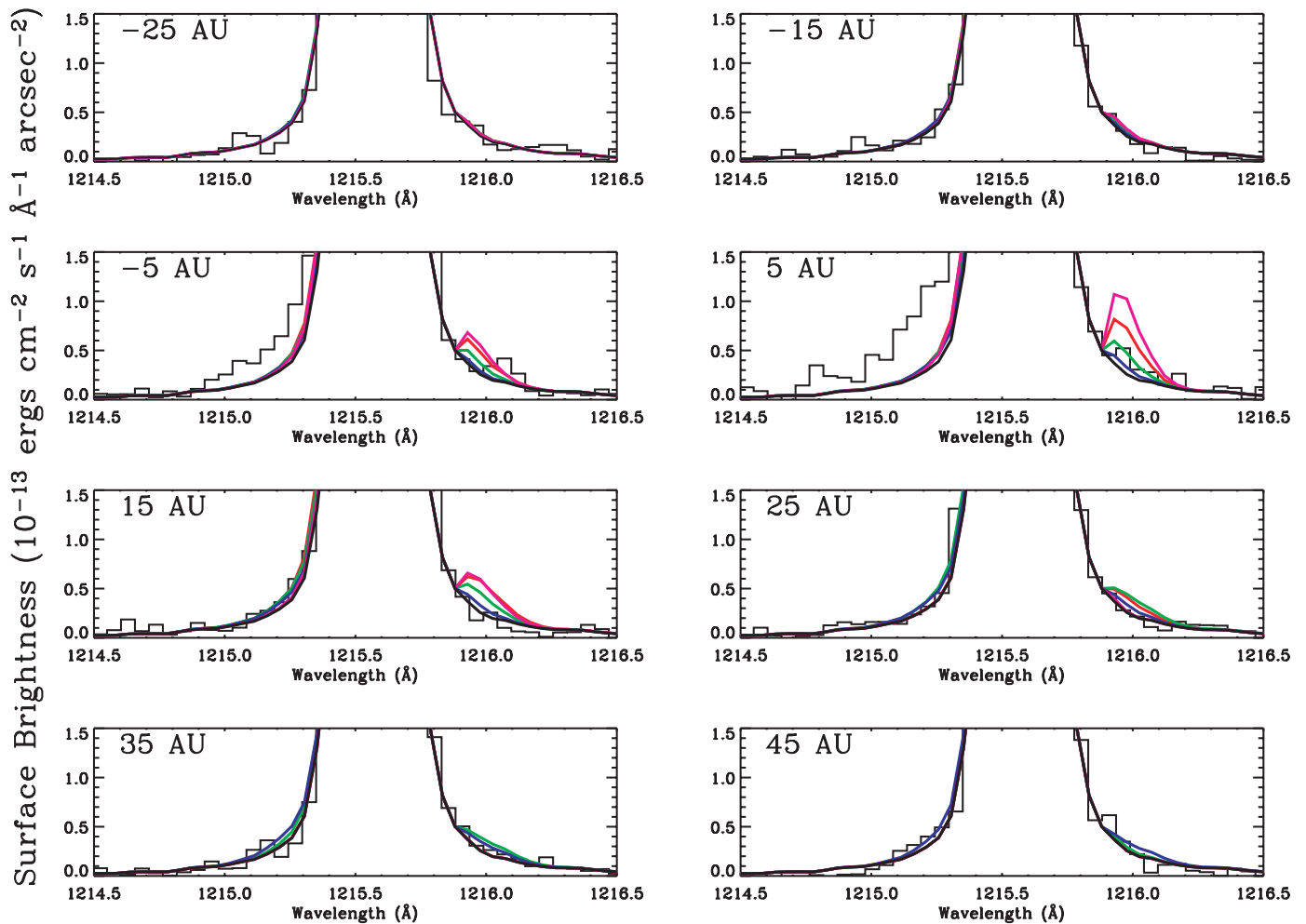


FIG. 8.—Comparison of the 40 Eri A Ly $\alpha$  spectrum observed by *HST*/STIS (entirely geocoronal emission; see Fig. 1) with the predictions of the  $0.5 \dot{M}_{\odot}$  (light purple lines),  $1 \dot{M}_{\odot}$  (red lines),  $2 \dot{M}_{\odot}$  (green lines), and  $5 \dot{M}_{\odot}$  (blue lines) models shown in Fig. 2, for eight positions along the slit, where positive distances are for the upwind direction of the ISM flow. The smooth black solid line is our best estimate of the shape of the geocoronal profile, which accounts for all the observed emission except for some stellar emission near the star at  $\pm 5$  AU. The  $0.5$ – $2 \dot{M}_{\odot}$  models suggest that we *should* have detected astrospheric emission as an excess in the red wing of the geocoronal profile at 5–25 AU, but we did not (see text).

previous *HST*/GHRS observations that yielded a tentative detection of astrospheric Ly $\alpha$  absorption toward 40 Eri A. However, the new STIS observations failed to detect any astrospheric emission. We have computed hydrodynamic models of the 40 Eri A astrosphere to see how much Ly $\alpha$  absorption and emission the models predict should be seen in the *HST* observations. Models with assumed mass-loss rates of  $\dot{M} \gtrsim 2 \dot{M}_{\odot}$  suggest that we should see more absorption than we actually observe, while models with assumed mass-loss rates of  $\dot{M} \lesssim 2 \dot{M}_{\odot}$  predict that our attempt to detect astrospheric emission should have been successful.

One might conservatively consider the borderline  $\dot{M} = 2 \dot{M}_{\odot}$  model to be marginally consistent with both the absorption data (see Fig. 4) and the emission data (see Fig. 8). Ironically, the mass loss versus activity relation derived by Wood et al. (2002) suggests that 40 Eri A should indeed have a mass-loss rate of  $\dot{M} \approx 2 \dot{M}_{\odot}$ . Nevertheless, the merely marginal consistency of the  $\dot{M} = 2 \dot{M}_{\odot}$  model with *both* the absorption and emission data leads us to consider other possibilities. Another possible interpretation is that the mass-loss rate of 40 Eri A could be a lot lower than the modeled range, since at some point astrospheric emission

must start *decreasing* with decreasing mass-loss rates, rather than increasing. If the mass-loss rate is sufficiently low, the astrosphere will be so optically thin to Ly $\alpha$  emission that it becomes dim and undetectable. However, the substantial amount of emission predicted for the  $\dot{M} = 0.5 \dot{M}_{\odot}$  model (see Fig. 8) suggests that the mass-loss rate for 40 Eri A would have to be much lower for this to work, and we see no reason to believe that 40 Eri A would have such a low mass-loss rate. (Note once again the  $\dot{M} = 2 \dot{M}_{\odot}$  prediction from the mass-loss/activity relation of Wood et al. 2002.)

A final possible explanation for our results, which we believe is the best interpretation, is that perhaps 40 Eri A lies outside the local cloud and is surrounded by the hot, completely ionized ISM material of the Local Bubble (see § 1). In this scenario, there is no neutral hydrogen in the surrounding ISM and therefore no astrospheric Ly $\alpha$  emission *or* absorption for us to detect. This interpretation would mean that the tentative detection of astrospheric absorption discussed in § 2 cannot be right. A model of the local cloud's shape presented by Redfield & Linsky (2000) implies a distance to its edge toward 40 Eri A of only 2.5 pc, half the stellar distance of 5.0 pc. This result is not definite because

of the assumptions that Redfield & Linsky (2000) must make to construct their model (e.g., uniform cloud density, etc.), but it does suggest that 40 Eri A could indeed be beyond the local cloud and within the hot ISM. *Thus, given the questionable nature of the previously reported absorption detection, and considering that our models seem to predict either too much absorption or too much emission, we believe that the models contradict the tentative detection of absorption and imply that the ISM surrounding 40 Eri A may be fully ionized.*

In the future, we intend to develop and apply more sophisticated codes for modeling astrospheres and our heliosphere. For example, we intend to expand the models from two to three dimensions, and we will also include MHD effects. When these models are available we can repeat the analysis presented here to see whether our conclusions change, but for now we conclude that 40 Eri A should be removed from the list of stars with detected astrospheres. The upper limit derived for its mass-loss rate from the now discredited absorption detection is also invalidated. However, since this mass-loss measurement is only an upper limit, our removal of 40 Eri A from consideration does not change any of the quantitative or qualitative conclusions of Wood et al. (2002) regarding how mass loss varies with activity and stellar age.

The 40 Eri A example emphasizes a fundamental difficulty in trying to study stellar winds from astrospheric Ly $\alpha$  data. Without a clear astrospheric detection absolutely nothing can be said about the stellar wind. Not even an upper limit for the mass-loss rate can be derived because of the possibility that the star is within the hot ISM and therefore has no astrospheric H I to detect. Only an extremely detailed and accurate three-dimensional map of the distribution of H I in the local neighborhood could remove this problem. Such a map is not currently available and is difficult to obtain because of the ambiguity of assigning interstellar material detected in absorption to specific locations along the observed lines of sight.

We would like to thank the anonymous referee for useful comments on the paper. Support for this work was provided by NASA through grants NAG5-9041 and S-56500-D to the University of Colorado, and through grant number GO-08237.01-A from the Space Telescope Science Institute, which is operated by AURA, Inc., under NASA contract NAS5-26555. G. P. Z. and H.-R. M. would also like to acknowledge support from NSF-DOE grant ATM-0296114. H.-R. M. thanks the Bartol Research Institute at the University of Delaware, where all of his numerical work was carried out.

#### REFERENCES

- Adams, T. F., Hummer, D. G., & Rybicki, G. B. 1971, *J. Quant. Spectrosc. Radiat. Transfer*, 11, 1365
- Baranov, V. B., & Malama, Y. G. 1993, *J. Geophys. Res.*, 98, 15157
- . 1995, *J. Geophys. Res.*, 100, 14755
- Bond, H. E., Mullan, D. J., O' Brien, M. S., & Sion, E. M. 2001, *ApJ*, 560, 919
- Dring, A. R., Linsky, J., Murthy, J., Henry, R. C., Moos, W., Vidal-Madjar, A., Audouze, J., & Landsman, W. 1997, *ApJ*, 488, 760
- Gayley, K. G., Zank, G. P., Pauls, H. L., Frisch, P. C., & Welty, D. E. 1997, *ApJ*, 487, 259
- Hummer, D. G. 1962, *MNRAS*, 125, 21
- Izmodenov, V. V., Lallement, R., & Malama, Y. G. 1999, *A&A*, 342, L13
- Kneer, F. 1975, *ApJ*, 200, 367
- Lindler, D. 1999, *CALSTIS Reference Guide (Greenbelt: NASA/LASP)*
- Linsky, J. L. 1998, *Space Sci. Rev.*, 84, 285
- Linsky, J. L., & Wood, B. E. 1996, *ApJ*, 463, 254
- Moos, H. W., et al. 2002, *ApJS*, 140, 3
- Müller, H.-R., Zank, G. P., & Wood, B. E. 2001, *ApJ*, 551, 495
- Piskunov, N., Wood, B. E., Linsky, J. L., Dempsey, R. C., & Ayres, T. R. 1997, *ApJ*, 474, 315
- Redfield, S., & Linsky, J. L. 2000, *ApJ*, 534, 825
- Sfeir, D. M., Lallement, R., Crifo, F., & Welsh, B. Y. 1999, *A&A*, 346, 785
- Wood, B. E., Alexander, W. R., & Linsky, J. L. 1996, *ApJ*, 470, 1157
- Wood, B. E., Ambruster, C. W., Brown, A., & Linsky, J. L. 2000a, *ApJ*, 542, 411
- Wood, B. E., & Karovska, M. 2000, *ApJ*, 543, 922
- Wood, B. E., & Linsky, J. L. 1998, *ApJ*, 492, 788
- Wood, B. E., Linsky, J. L., Müller, H.-R., & Zank, G. P. 2001, *ApJ*, 547, L49
- Wood, B. E., Linsky, J. L., & Zank, G. P. 2000b, *ApJ*, 537, 304
- Wood, B. E., Müller, H.-R., & Zank, G. P. 2000c, *ApJ*, 542, 493
- Wood, B. E., Müller, H.-R., Zank, G. P., & Linsky, J. L. 2002, *ApJ*, 574, 412
- Zank, G. P., Pauls, H. L., Williams, L. L., & Hall, D. T. 1996, *J. Geophys. Res.*, 101, 21639